Mecanosíntesis de
polvos nanocristalinos de CaTi$_{1-x}$Mn$_x$O$_{3-\delta}$

P. GONÇALVES [1], J. CANALES-VÁZQUEZ [2], F. M. FIGUEIREDO [1,3]

[1] Ceramics and Glass Engineering Dep, CICECO, University of Aveiro, 3810 Aveiro, Portugal
[2] Renewable Energy Research Institute, Universidad de Castilla la Mancha, 02006 Albacete, Spain
[3] Science and Technology Dep, Universidade Aberta, P. da Escola Politécnica 147, 1269-001, Lisboa, Portugal

La mecanosíntesis de CaTi$_{1-x}$Mn$_x$O$_{3-\delta}$ nanocristalino es presentada por primera vez. Polvos reactivos de CaO, TiO$_2$ anatasa y Mn$_2$O$_3$ (Aldrich) fueron pesados en las cantidades estequiométricas adecuadas para obtener CaTi$_{1-x}$Mn$_x$O$_{3-\delta}$ (x=0.05, 0.10, 0.15, 0.20, 0.30, 0.50 y 0.80) por molienda en seco en un molino planetario de alta energía utilizando contenedores y bolas de circona, en una relación masa de bolas : masa de polvo de 10:1. La rotación del planetario se mantuvo constante a 650 revoluciones por minuto (rpm) y la del contenedor a 1300 rpm, en el sentido inverso. La formación de una fase con estructura de perovskita fue identificada a través del análisis de los polvos por difracción de rayos X, siendo esta fase claramente mayoritaria en los polvo molidos durante 180 min y sin observarse la formación de compuestos intermediarios. Los patrones de difracción de rayos X también indicaron una disminución de los parámetro de red con el aumento del contenido en Mn, en acuerdo con el menor rayo iónico de Mn^{3+} o Mn^{4+} comparado con el del catión Ti^{4+}. El tamaño medio de los cristales fue estimado entre 5 y 30 nm a partir de gráficos de Williamson-Hall y confirmado por microscopia electrónica de transmisión.

Palabras clave: Conductor mixto, titanato, mecanosíntesis.

Mechanosynthesis of nanocrystalline CaTi$_{1-x}$Mn$_x$O$_{3-\delta}$

The mechanosynthesis of nanocrystalline CaTi$_{1-x}$Mn$_x$O$_{3-\delta}$ is reported for the first time. Powdered CaO, TiO$_2$ anatase and Mn$_2$O$_3$ (Aldrich) were weighed in the appropriate stoichiometric quantities in order to obtain CaTi$_{1-x}$Mn$_x$O$_{3-\delta}$ (x=0.05, 0.10, 0.15, 0.20, 0.30, 0.50 and 0.80) and dry milled in a planetary high-energy ball mill, using zirconia containers and balls, with a 10:1 ball/mass ratio. The planetary rotation was kept constant at 650 rpm and the container at 1300 rpm, in the opposite direction. Powder XRD patterns revealed a perovskite forming from the early milling stages and a completed reaction after 180 min, with no apparent crystalline or amorphous intermediates, indicating significant Mn solubility in CaTiO$_3$. Patterns show a decrease in lattice volume upon Mn substitution, as expected from the lower Mn^{3+} or Mn^{4+} ionic radii when compared to Ti^{4+}. The average crystallite size is in the range 5-30 nm, as determined from Williamson-Hall plots and confirmed by high resolution transmission electron microscopy.

Keywords: mixed conductor, titanate, mechanosynthesis.

1. INTRODUCTION

It is well-known that the partial substitution of Ti^{4+} by Fe transforms the incipient ferroelectric CaTiO$_3$ into a good oxygen ionic/electronic mixed conductor (1-4). The partial substitution of Ti^{4+} by lower-valence Fe^{3+} cations enhances the concentration of electron holes and oxygen vacancies (V$_O^{\bullet\bullet}$). However, a proportion of these vacancies tends to order in FeO$_4$ tetrahedra chains perpendicular to the c-axis (5,6) while the rest remain disordered around pentacoordinated Fe^{3+}. (7,8) Thus, the ionic conductivity of these materials depends on the concentration of ordered and disordered V$_O^{\bullet\bullet}$, which exhibit significantly different mobilities. Indeed, a maximum in the ionic conductivity of CaTi$_{1-x}$Fe$_x$O$_{3-\delta}$ is observed for x≈0.20. (1,3) Long-range ordering is eventually established when the V$_O^{\bullet\bullet}$ concentration is high enough, and new phases with the general formula A$_n$B$_n$O$_{3n-1}$, which consist of a succession of alternating BO$_6$ octahedra and BO$_4$ tetrahedra layers, can be formed. (5,6).

These materials, in particular CaTi$_{1-x}$Fe$_x$O$_{3-\delta}$ (x in the range 0.2–0.3), combine a satisfactory chemical stability with a moderate thermal expansion coefficient (≈12x 10^{-6} K^{-1}) and reasonably good transport properties, and were thus envisaged for application as membranes for electrochemical oxygen separation (9) or hydrogen production. (10) Nevertheless, the ionic transport is recognised to be somewhat limited and any improvement of this characteristic is important for the actual technological application of the material.

Obvious attempts to improve the transport properties of CaTiO$_3$ based mixed conductors include doping with a different transition metal such as Co or Ni. Indeed, attempts were made but these seem to have failed due to formation of secondary phases resulting from the low solubility of such cations in the CaTiO$_3$ lattice (1). Recently published atomistic simulations indicate that Mn^{3+} solution and defect association energies in the CaTiO$_3$ lattice are favourable and should, in principle, lead to a higher ionic conductivity than in the Fe-doped material (11). Surprisingly, to the best of our knowledge, very little is known about any intermediate solid solutions or phases (if they exist at all) in the CaTiO$_3$-CaMnO$_{3-\delta}$ system, although the

Bol. Soc. Esp. Ceram. V., 47, 4, 233-237 (2008)

233

end members are relatively well characterised (6,7,12).

This work reports a successful attempt to synthesise Mn-substituted $CaTiO_3$ nanoparticles by room temperature mechanosynthesis.

2. EXPERIMENTAL PROCEDURE

Anatase TiO_2, Mn_2O_3 and CaO (Sigma Aldrich) powders were calcined separately at 1000°C for 10-12h and dosed in the stoichiometric quantities corresponding to $CaTi_{1-x}Mn_xO_{3-1/2x}$ (x=0, 0.05, 0.10, 0.15, 0.20, 0.30, 0.50 and 0.80). The milling experiments were carried out in a Retsch PM 200 planetary ball mill with constant planetary and container rotation of 650 and 1300 rotations per minute (rpm), respectively, using zirconia vials (125 cm^3) and tetragonal zirconia balls (Tosho co.) in a ball:powder ratio of 10:1. Excess heating was avoided by milling for periods of 5 minutes and subsequently pausing for the same period of time. The rotation was reversed after each interruption.

The reaction was monitored by X-ray diffraction (XRD) analysis of powder samples collected after 60 minutes pausing, using a Rigaku Geigerflex diffractometer (CuK_α radiation, scan rate 3º/min). The strain and diffracting volume contributions to peak broadening were assessed by an integral breadth method based on Williamson-Hall plots (13). The experimental width was corrected based on data collected for LaB_6 and Si standard references.

Microstructure and chemical homogeneity were analysed by scanning and transmission electron microscopy (SEM and TEM) coupled to energy dispersive X-ray spectroscopy (EDS) analyses performed in a Hitachi 4100S SEM and a JEOL 2011 transmission electron microscope operating at 200 kV, both equipped with EDS detectors. The powder samples for TEM analysis were dispersed in acetone and deposited on a carbon coated perforated copper grid.

The level of zirconium contamination was found to be consistently below 0.45 mass % for all samples, as determined by inductively coupled plasma atomic emission spectroscopy (ICP-AES) analysis of solutions containing the milled powders dissolved with nitric acid in an ultrasonic bath, carried out in a Jobin Yvon 70 Plus spectrometer (Horiba Jobin Yvon Inc., Edison, NJ, USA).

3. RESULTS AND DISCUSSION

Figure 1 depicts the evolution of the phase formation during the milling of a mixture of calcia, anatase and manganese oxide at 650 rpm. The changes observed in the diffraction pattern of the fresh mixture after milling for 1 hour are remarkable, especially the significant decrease of the intensity of all initial peaks and the onset of new diffraction maxima near 2θ values corresponding to $CaTiO_3$. The perovskite totally dominates the pattern collected after 120 min and further milling leads to a substantial increase in intensity of the perovskite maxima, with no evidence of any secondary phases or amorphous intermediates. This behaviour is typical for the entire, fairly broad, compositional range studied.

The final 180 min XRD patterns are shown in Figure 2, for increasing Mn contents up to 80 mol%. No secondary phases were detected, in agreement with the expected good solubility of Mn^{3+} in the $CaTiO_3$ lattice (10). The shift of the perovskite

diffraction maxima to higher angles, apparent with increasing manganese content, suggests a decrease in lattice volume upon Mn substitution, in agreement with partial substitution of Ti^{4+} for smaller Mn^{3+} cations, and also Mn^{4+}. All patterns show a very similar trend for x ≤ 0.3, whilst for x=0.5 and 0.8 the intensity is lower, perhaps indicating less developed crystallites for the higher manganese contents.
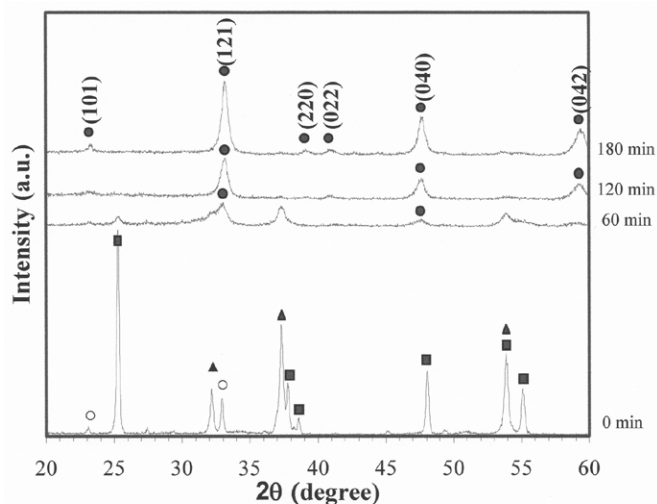

Fig. 1- Evolution of powder XRD patterns with milling time for the exemplificative $CaTi_{0.8}Mn_{0.2}O_{3-\delta}$ composition. The markers identify a (●) perovskite phase, (■) anatase (PDF#73-1764), (▲) calcia (PDF#48-1467) and (○) manganese III oxide (PDF#24-0508).
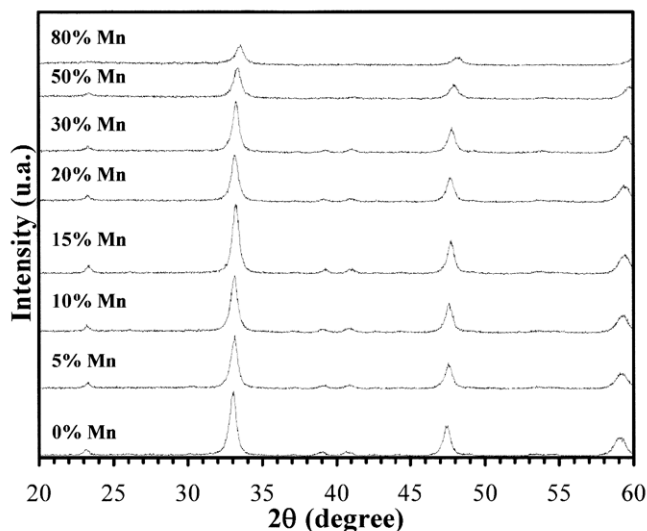

Fig. 2- Powder XRD patterns for $CaTi_{1-x}Mn_xO_{3-\delta}$ mixtures milled for 180 min.

A significant peak broadening is apparent in all patterns, which may be due to a combined effect of crystallite size, in the nanometer range, and lattice strain, both resulting from high-energy milling. The Scherrer formula yields unreasonably small average crystallite sizes of the order of a few Ångström, which means that the observed peak broadening is too large to be explained only by simple size effects. The contribution of

234

Bol. Soc. Esp. Ceram. V., 47, 4, 233-237 (2008)

lattice strain induced by mechanical milling may be taken into account with an integral breadth method and assuming the relation between the crystallite size, expressed as the apparent average diameter ε, and the mean lattice strain, η, given by

$$\left(\frac{\beta^*}{d^*}\right)^2 \approx \frac{1}{\varepsilon}\frac{\beta^*}{\left(d^*\right)^2}+\left(\frac{\eta}{2}\right)^2, \qquad [1]$$

where β^* is the integral breadth and d^* the interplanar distance, both in reciprocal space units (12). The representation of β^* and d^* according to Equation [1], known as a Williamson-Hall plot, is depicted in Figure 3 for x=0.15 and 0.80 powders milled for 180 min, as an example. The agreement with Equation 1 is fair for x ≤ 0.30 yielding apparently coherent ε and η estimations. As expected, the crystallite size increases with increasing milling time up to maximum values in the order of 25-30 nm, as shown for some materials in Figure 4. On the other hand, the mean apparent strain, expressed as a root mean square strain, $e_{rms} \approx \eta / 5$ (13), was found to be nearly independent of composition within the range between e_{rms}=0.001 to 0.003 for x≤0.30. It should be noticed, however, that the dispersion affecting these sets of data is considerable and that the expected relative errors affecting ε estimates are in the range between 13 and 49%. This may be due to a broad distribution of crystallite sizes, as discussed further on over the TEM results. The quality of the fit to the x=0.50 and 0.80 data was much less satisfactory, showing, besides poor regression coefficients, meaningless negative intercepts, although very small and probably resulting from data dispersion. The failure to fit these data may be explained, amongst other causes, by poorly developed phases, yielding poorly resolved patterns, or by a pattern resulting from the contribution of different phases with similar structures and similar lattice parameters, e.g. phases isostructural to $CaMnO_3$, $CaMnO_{2.8}$, $CaMnO_{2.75}$ or $CaMnO_{2.5}$. (12) Nevertheless, it was possible to obtain ε estimates. Figure 5 depicts the evolution of the average crystallite size determined from the XRD patterns as a function of the manganese molar fraction. It can be seen that ε consistently decreases from about 28 nm for x≤0.15 to ≈11 nm for x=0.80.
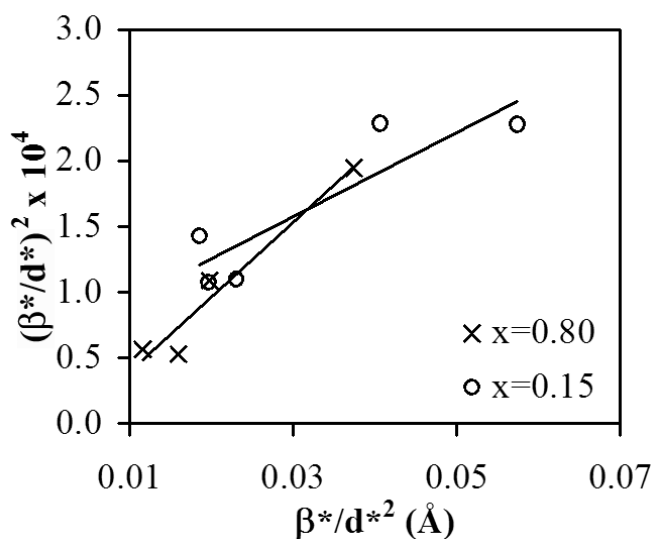

Fig. 3- Typical Williamson-Hall plots, shown for the x=0.05 and 0.80 compositions.
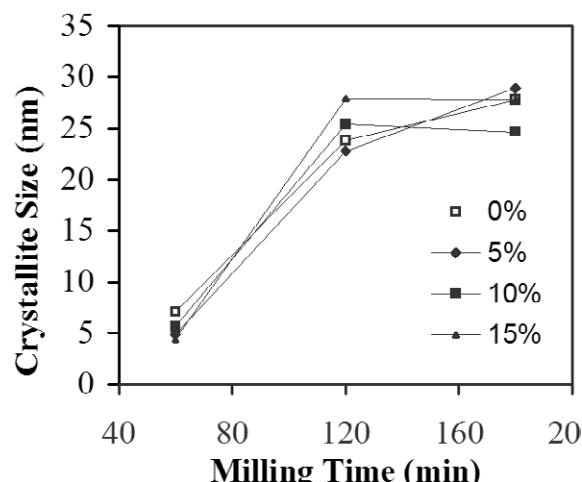

Fig. 4- Average crystallite size determined from XRD patterns plotted as a function of milling time.
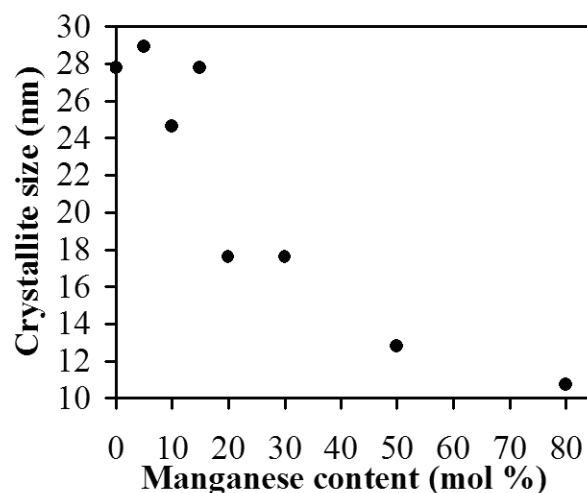

Fig. 5- Average crystallite size determined from XRD patterns plotted as a function of Mn content.

Electron microscopy studies were conducted to detail the microstructure of the powders. Figure 6 shows SEM micrographs illustrating a strongly agglomerated powder consisting of nanosized particles/crystallites. There are no apparent differences between the various compositions. The SEM study was complemented with more informative HRTEM. Two typical micrographs are shown in Figure 7 for samples with low (x=0.05) and high (x=0.50) Mn content. These images generally confirm the XRD results showing well-crystallised materials for lower Mn fractions, with a broad crystallite size range 5-20 nm (Figure 7(A)) that is coherent with the dispersion observed in the Williamson-Hall plots. In the case of the phases with high Mn fraction, there is clear evidence for highly disordered particles for x=0.5 (Figure 7(B)) and, in particular for the 80 mol % composition (not shown). The crystallites are clearly smaller than for x≤0.30 Mn contents, although it is difficult to categorically infer an approximate size due to poor crystallinity.

The powder XRD patterns shown above are typical from a cubic phase, although the orthorhombic structure of the parent compound ($CaTiO_3$) would suggest the new compounds to have a structure with lower symmetry. Indeed, a careful
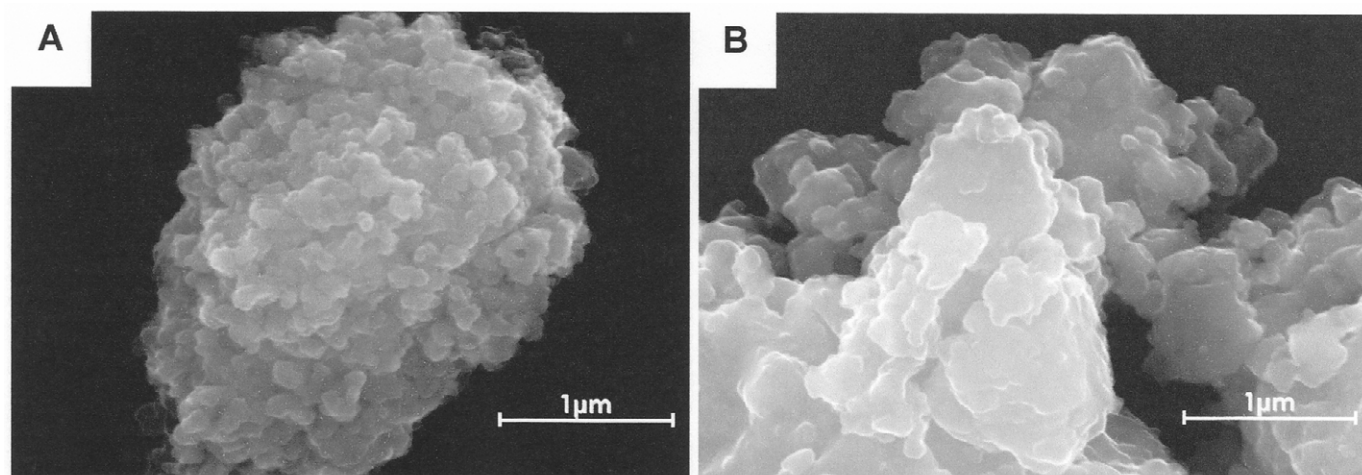
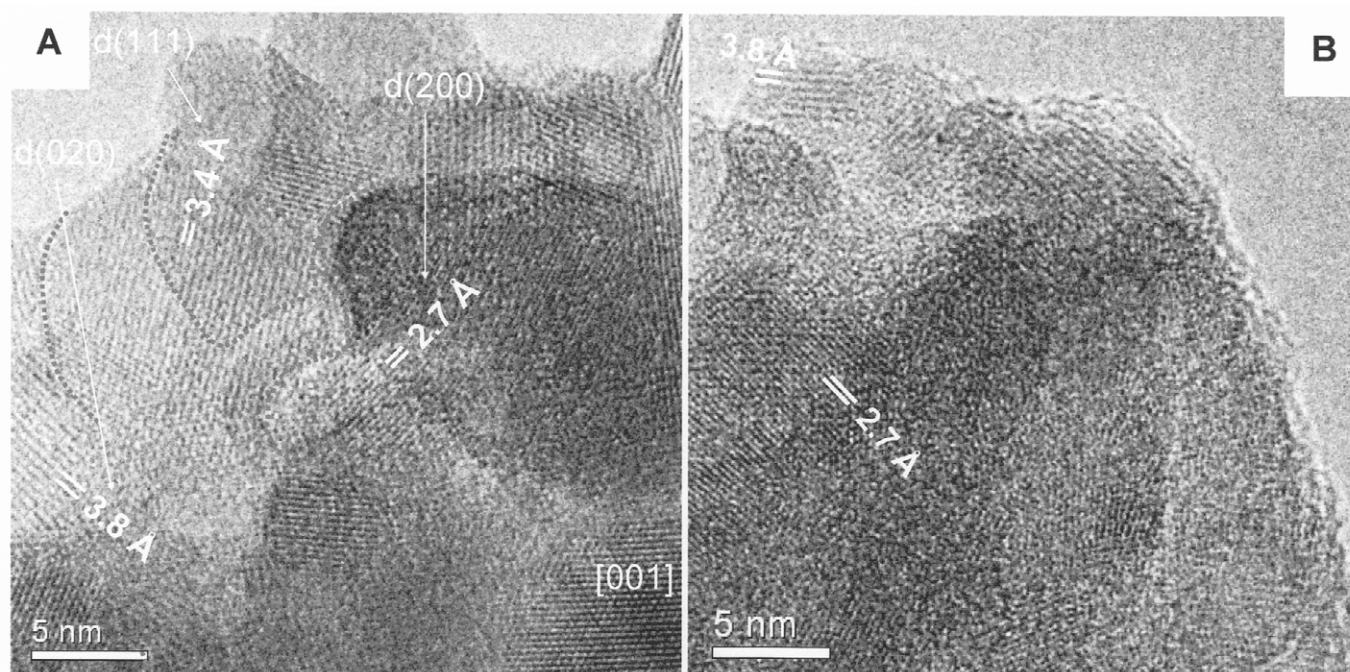Fig. 6- SEM micrographs corresponding to (A) x=0.15 and (B) x=0.80.

Fig. 7- HRTEM images collected for (A) x=0.05 and (B) x=0.50 samples milled for 180 min.

HRTEM analysis revealed d-spacing values of 0.34 nm (Figure 7(A)), which cannot be explained by a simple cubic structure, but may be indexed to the (111) plane of the orthorhombic Pbnm space group of $CaTiO_3$. In fact, all images can be indexed onto this space group. This is a reasonable assumption for x≤0.30 (or even <0.50), but it is unlikely for the materials with higher Mn content, which may, for instance, favour rhombohedral symmetry. These issues certainly demand for future confirmation.

4. CONCLUSIONS

The mechanosynthesis of nanocrystalline $CaTi_{1-x}Mn_xO_{3-\delta}$ was demonstrated for the first time starting from CaO, TiO_2 anatase and Mn_2O_3 using a planetary high energy ball-mill at 650 rpm planetary rotation and container at 1300 rpm. A final X-ray single phase nanocrystalline (5-30 nm) product was obtained after milling for 180 min, with no apparent crystalline or amorphous intermediates. The results indicate significant Mn solubility in $CaTiO_3$ and a decrease in lattice volume upon Mn substitution, as expected from the lower Mn^{3+} or Mn^{4+} ionic radii and in agreement with previous atomistic simulations.

Future work will involve the processing of these powders into dense ceramic bodies and the study of their transport properties. This will certainly involve high temperature treatments that may affect Mn solubility. On the other hand, a detailed structural study by HRTEM/SAED and techniques which allow for the determination of the oxidation state and coordination of the Mn cations, e.g. magnetic measurements and oxygen stoichiometry measurements, will be necessary to elucidate the real structure of these phases as defect ordering (in particular oxygen vacancies) is likely to occur leading to formation of complex extended defects.

ACKNOWLEDGEMENTS

REFERENCES

1. H. Iwahara, T. Esaka, T. Mangahara, Mixed conduction and oxygen permeation in the substituted oxides for CaTiO$_3$, J. Appl. Electrochem., 18, 173-177 (1988).

2. V.V. Lemanov, A.V. Sotnikov, E.P. Smirnova, M. Weihnacht, R. Kunzeb, Perovskite CaTiO$_3$ as an incipient ferroelectric, Solid State Communications, 110, 611–614 (1999).

3. F.M. Figueiredo, J.C. Waerenborgh, V.V. Kharton, H. Näfe, J.R. Frade, On the relationships between structure, oxygen stoichiometry and ionic conductivity of CaTi$_{1-x}$Fe$_x$O$_{3-\delta}$ (x=0.05, 0.20, 0.40, 0.60), Solid State Ionics, 156, 371-381 (2003).

4. F.M. Figueiredo, V.V. Kharton, J.C. Waerenborgh, A.P. Viskup, E.N. Naumovich, J.R. Frade, Influence of Microstructure on the Electrical Properties of Iron-Substituted Calcium Titanate Ceramics, J. Am. Ceram. Soc., 87, 12, 2252–2261 (2004).

5. J.-C. Grenier, G. Schiffmacher, P. Caro, M. Pouchard, P. Hagenmuller, Étude par Diffraction X et Microscopie Electronique du Système CaTiO$_3$–Ca$_2$Fe$_2$O$_5$ (Study of the CaTiO$_3$–Ca$_2$Fe$_2$O$_5$ System by X-ray Diffraction and Electron Microscopy) (in French), J. Solid State Chem., 20, 365–379 (1977).

6. J.-C. Grenier; M. Pouchard, P. Hagenmuller, G. Schiffmacher, P. Caro, Ordre–De´sordre des Lacunes Anioniques dans les Perovsquites Non Stoechiome´triques CaTi$_{1-2y}$Fe$_{2y}$O$_{3-y}$ (Order–Disorder of Anionic Vacancies in Non-Stoichiometric Perovskites CaTi$_{1-2y}$Fe$_{2y}$O$_{3-y}$) (in Fr.), J. Phys. Colloq., C7, 38, C7/84–C7/89 (1977).

7. C. McCammon, A.I. Becerro, F. Langenhorst, R. Angel, S. Marion, F. Seifert, Short-Range Ordering of Oxygen Vacancies in CaFe$_x$Ti$_{1-x}$O$_{3-x/2}$ Perovskites (0<x<0.4), J. Phys.: Condens. Matter B, 12, 2969–2984 (2000).

8. J.C. Waerenborgh, F.M. Figueiredo, J.R. Jurado, J.R. Frade, Fe^{4+} Content and Short-Range Ordering of Anion Vacancies in Partially Reduced AFe$_x$Ti$_{1-x}$O$_{3-y}$ (A=Ca, Sr; x≤0.6) Perovskites. An ^{57}Fe Mössbauer Spectroscopy Study J. Phys.: Condens. Matter B, 13, 8171–8187 (2001).

9. H. Itoh, H. Asano, K. Fukuroi, M. Nagata, and H. Iwahara, Spin Coating of a Ca(Ti,Fe)O3 Dense Film on a Porous Substrate for Electrochemical Permeation of Oxygen, J. Am. Ceram. Soc., 80, 6, 1359–1365 (1997).

10. T. Esaka, T. Fujii, K. Suwa, H. Iwahara, Electrical Conduction in CaTi$_{1-x}$Fe$_x$O$_{3-\delta}$ Under Low Oxygen Pressure and its Application for Hydrogen Production, Solid State Ionics, 40/41, 544–547 (1990).

11. G.C. Mather, M.S. Islam, F.M. Figueiredo, Atomistic Study of a CaTiO$_3$-Based Mixed Conductor: Defects, Nanoscale Clusters, and Oxide-Ion Migration, Adv. Funct. Mater., 17, 905–912 (2007).

12. E. Bakken, J. Boerio-Goates, T. Grande, B. Hovde, T. Norby, L. Rørmark, R. Stevens, S. Stølen, Entropy of oxidation and redox energetics of CaMnO$_{3-\delta}$, Solid State Ionics, 176, 2261 – 2267 (2005).

13. J.I. Langford, in: Defect and Microstructure Analysis by Diffraction, edited by P. Snyder, F. Fiala and H. Bunge, volume 10 of IUCr Monographs on Crystallography, pages 59–81, Oxford University Press, Oxford (1999).

◆ ◆ ◆

Bol. Soc. Esp. Ceram. V., 47, 4, 233-237 (2008)

237